Nuclear Inst. and Methods in Physics Research, A 1039 (2022) 167093

Contents lists available at ScienceDirect

Nuclear Inst. and Methods in Physics Research, A

journal homepage: www.elsevier.com/locate/nima

Design and commissioning of an e-beam irradiation beamline at the Upgraded Injector Test Facility at Jefferson Lab

Xi Li [a,*], Helmut Baumgart [a,c,**], Charles Bott [e,f], Gianluigi Ciovati [b,*], Shaun Gregory [b], Fay Hannon [d], Mike McCaughan [b], Robert Pearce [e,f], Matthew Poelker [b], Hannes Vennekate [b], Shaoheng Wang [b]

[a] Department of Electrical and Computer Engineering, Old Dominion University, Norfolk, VA 23529, United States
[b] Thomas Jefferson National Accelerator Facility, Newport News, VA 23606, United States
[c] Applied Research Center at Thomas Jefferson National Accelerator Facility, Newport News, VA 23606, United States
[d] Phase Space Tech, Norra Villavagen 30, 23734 Bjarred, Sweden
[e] Hampton Roads Sanitation District, Virginia Beach, VA 23455, United States
[f] Department of Civil and Environmental Engineering, Virginia Tech, Blacksburg, VA 24061, United States

ARTICLE INFO

Keywords:
Electron beam irradiation
Absorbed dose calculation
Dose distribution
Superconducting radio-frequency accelerator

ABSTRACT

The Upgraded Injector Test Facility (UITF) at Jefferson Lab is a continuous-wave superconducting linear accelerator capable of providing an electron beam with energy up to 10 MeV. A beamline for electron-beam irradiation has been designed, installed and successfully commissioned at this facility, aimed at the degradation study of 1,4-dioxane and per- and polyfluoroalkyl substances (PFAS) in wastewater treatment. A solenoid with a peak axial magnetic field of up to 0.28 T and a set of raster coils were used to obtain a Gaussian beam profile with a transverse standard deviation of ∼15.0 mm at the target location. Monte-Carlo simulations using FLUKA were carried out to calculate the total absorbed dose and the dose distribution in the sample volume inside the target cell. The simulations were benchmarked experimentally by dosimetry mapping using opti-chromic dosimeters. The results of the irradiation experiments showed a ∼95% reduction of 1,4-dioxane in ultra-pure water for a dose of 1 kGy, demonstrating the potential of electron-beam irradiation towards addressing growing challenges in environmental remediation.

1. Introduction

Electron beam (EB) irradiation is a material processing method that has many industrial applications, including environmental remediation such as the treatment of flue gases and wastewater [1–5]. In the case of EB irradiation of wastewater, the interaction between high energy electrons and water molecules produces mainly two reducers (aqueous electron and hydrogen radical) and one oxidant (hydroxyl radical) [6]. These free radicals initiate further oxidation/reduction processes in the wastewater which can remove many harmful pollutants including toxic chemicals, bacteria, viruses, and pathogens [7]. Recent studies have shown that EB irradiation is a promising method for reducing common harmful organic compounds such as per- and polyfluoroalkyl substances (PFAS) [8–13] which are difficult to remove by conventional treatment methods [14]. 1,4-dioxane [15] is another ubiquitous harmful chemical in wastewater for which there is no well-established removal method. Novel, efficient treatment techniques are in high demand as some of these compounds may soon be subjected to regulation by the U.S. Environmental Protection Agency [16]. The availability of research facilities in the US for electron beam irradiation studies is very limited, slowing the pace of technical advances towards developing improved accelerator-based facilities and investigating the effectiveness of EB irradiation for industrial applications.

The electron accelerators being used for EB irradiation at a few wastewater treatment facilities worldwide are DC, transformer-type accelerators [17–20], with a beam energy of up to a few MeV and a beam power in the tens to hundreds of kW. A higher beam power at high efficiency and a beam energy up to 10 MeV are desired to increase the wastewater processing volume, therefore reducing the treatment cost [21]. A higher beam power also allows increasing the dose, which could help in reducing or eliminating more recalcitrant chemicals. Superconducting radiofrequency (SRF) accelerators are significantly more efficient than normal-conducting ones and are widely used in large-scale accelerator facilities for scientific research throughout the world [22]. Recent advances in more efficient SRF cavities and cryogenic technologies could enable compact, cost-effective SRF

* Corresponding authors.
** Corresponding author at: Department of Electrical and Computer Engineering, Old Dominion University, Norfolk, VA 23529, United States.
E-mail addresses: xli009@odu.edu (X. Li), hbaumgar@odu.edu (H. Baumgart), gciovati@jlab.org (G. Ciovati).

https://doi.org/10.1016/j.nima.2022.167093
Received 12 March 2022; Received in revised form 3 June 2022; Accepted 24 June 2022
Available online 3 July 2022
0168-9002/

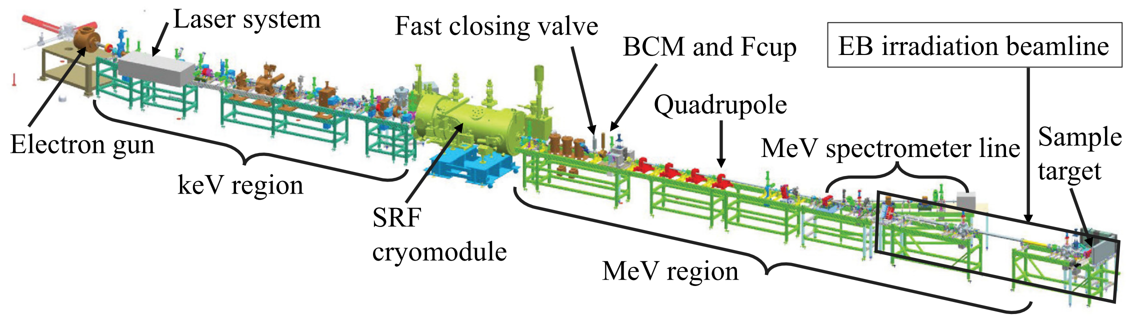

Fig. 1. Schematic layout of the UITF at Jefferson Lab. (BCM -- beam current monitor; Fcup -- Faraday cup.)

accelerators with significantly higher beam power and energy up to 10 MeV [23,24].

The aim of this work is to design, install and commission an EB irradiation beamline at the Upgraded Injector Test Facility (UITF) at Jefferson Lab in order to investigate the effect of EB irradiation on the removal of 1,4-dioxane and PFAS in wastewater samples, through a collaboration with local universities and the local wastewater treatment utility company. The UITF is a 10 MeV SRF, continuous wave (CW) accelerator, with a beam current of up to ∼1 mA which became operational at Jefferson Lab in 2020 [25]. Fig. 1 shows a schematic layout of the UITF. Electrons are produced from a DC high voltage photo-gun biased at up to 200 kV and driven by laser pulses at 780 nm with a pulse repetition rate of 748.5 MHz. The electron beam is then accelerated by a 1497 MHz SRF cryomodule consisting of a 2-cell Nb cavity that accelerates the electrons to relativistic energy and a 7-cell Nb cavity that accelerates the beam up to 10 MeV. The cavities are cooled to ∼2 K by a superfluid He bath inside the cryomodule. The EB irradiation beamline is ∼5 m long and it is located in a straight beamline section downstream of the MeV spectrometer beamline in Fig. 1. The radiation shielding currently installed around the accelerator administratively limits the beam current to 100 nA. The UITF accelerator will be described in greater detail in a future publication [25]. The two major design constraints considered for the irradiation beamline were a transverse beam diameter of ∼50 mm at the target location and a target sample volume of at least 50 mL. The constraint on the transverse beam diameter was applied in order to use a commercially available beam exit window. The constraint on the sample target volume was given by the minimum volume of water (∼40 mL) required for the analysis of 1,4-dioxane concentration. In addition, a beam energy for irradiation of 8 MeV was chosen as a conservative value, considering the maximum operating beam energy at UITF.

This article is organized as follows: the beamline design and beam transport simulations are described in Section 2; the main beamline components are described in Section 3. The results from the beamline commissioning are discussed in Section 4. The dosimetry study is presented in Section 5 and a summary is given in Section 6.

2. Beamline design and beam transportation simulation

Beam transport simulations were carried out using the computer code General Particle Tracer (GPT) [26], in order to determine the settings of the solenoid magnets in the keV region and of the quadrupoles and defocusing solenoid in the MeV region, resulting in a beam transverse diameter of ∼50 mm at the target location. Given the Gaussian distribution of the transverse beam profile, a σ of ∼8.3 mm is required, corresponding to a 3σ beam radius of about 25 mm.

Starting from the photocathode inside the electron gun, Fig. 2(a) shows a simulated end-to-end transverse beam envelope that provides the desired beam size at the sample target. Fig. 2(b) shows the beam envelope from the quadrupoles in the MeV region to the target. For the initial spatial distribution of the electron beam, the transverse σ of the beam was set equal to 1σ of the laser spot size which was measured to

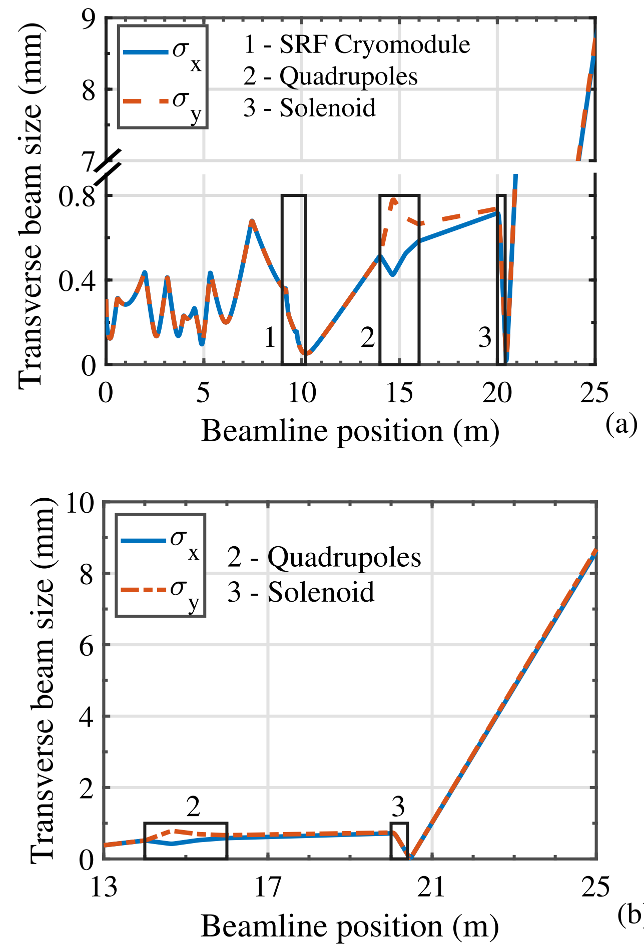

Fig. 2. Transverse beam size along the entire UITF beamline (a) and detailed view along the irradiation beamline (b) simulated with GPT.

be 0.325 mm. The initial electron bunch length was set to be equal to the laser temporal pulse whose full width at half maximum (FWHM) is measured to be 50 ps. In the simulation, the electrons were assumed to be emitted uniformly from the GaAs photocathode surface, and the initial momentum distribution was set to be uniform. The electron mean thermal energy was set to 0.04 eV, appropriate for the laser wavelength of 780 nm [27]. The bunch charge was set to 0.13 fC, which corresponds to a nominal average beam current of 100 nA at the bunch repetition rate of 748.5 MHz. The simulated normalized emittance of the electron beam was 0.09 π mm mrad, which is of the same order as results from emittance measurements made near the photo-gun [25]. The simulation also shows that there is no significant change in the emittance when space charge effects are included.

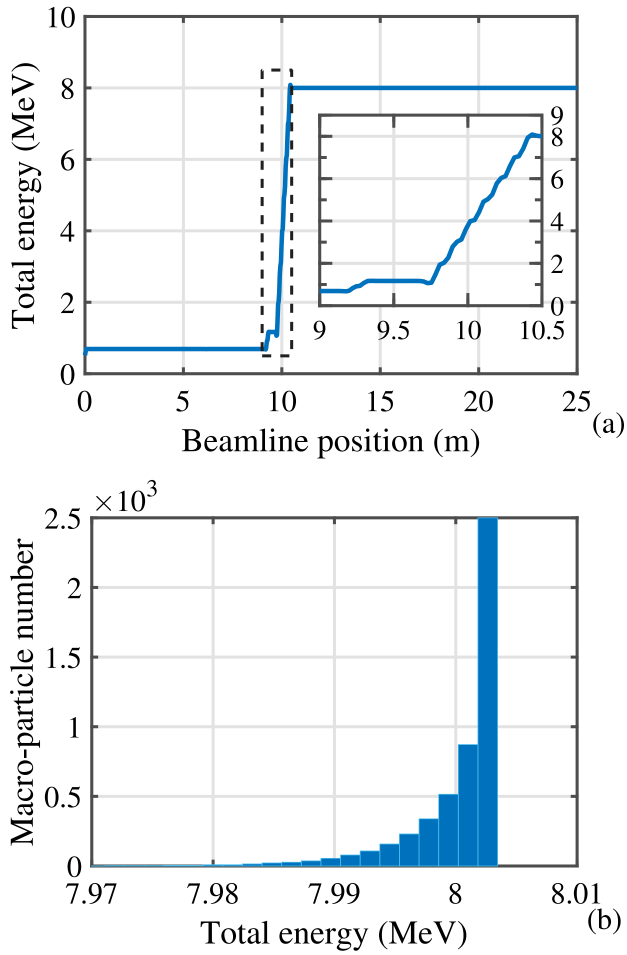

Fig. 3. Average total energy along the entire UITF beamline (a) and energy spread of the electron beam after the SRF cryomodule (b) simulated with GPT. The inset in (a) shows the total energy through the SRF cryomodule.

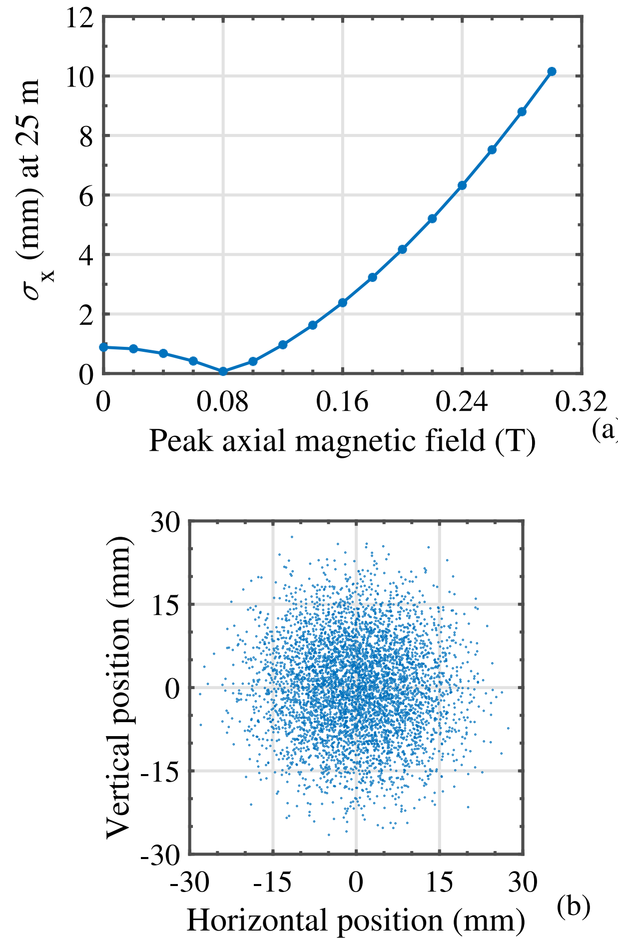

Fig. 4. (a) Transverse beam size at the sample target as a function of peak axial magnetic field of the defocusing solenoid and (b) transverse spatial distribution of the desired beam at the sample target for $B_0 = 0.28$ T from GPT simulation. The total beam energy is 8 MeV.

In simulation and in practice, the accelerating gradient and phase of the SRF cavities were set to provide "on-crest" acceleration of the beam to achieve an average total energy, E_b, of 8 MeV. The simulated relative energy spread was $\sim 10^{-4}$, of the same order as measured at the MeV spectrometer beamline [25]. The simulated electron beam energy along the beamline and the energy spread are shown in Fig. 3(a) and (b).

Unlike quadrupole magnets which focus the beam in one plane, the solenoid magnet in the EB irradiation line provided a simple mean to set the beam size at the water target in both planes. Located approximately 5 m from the sample target, the solenoid magnet provided a focal point a short distance downstream, such that the beam was diverging in the following drift space towards the target. The solenoid magnet provided some flexibility in the beam size at its entrance: as long as the beam size at the solenoid was kept below 1.2 mm, solenoid settings could be found to sufficiently blow up the beam to the desired size at the target. In practice, quadrupole magnet settings that provided a transverse $\sigma \simeq 0.8$ mm at the entrance to the solenoid worked best, providing the desired transverse $\sigma \simeq 8.5$ mm at the sample target, with a peak axial magnetic field $B_0 \sim 0.28$ T, as shown in Fig. 4(a). The transverse scattering plot of the desired electron beam at the sample target is shown in Fig. 4(b).

Our study showed that a larger transverse σ of the electron beam can improve the dose uniformity within the sample [28]. However, the desired 0.28 T peak axial magnetic field was close to the maximum operational value of the solenoid. In order to further increase the beam size at the sample target, a set of raster coils were installed downstream of the solenoid to produce two perpendicular dipole alternating current (AC) magnetic fields, with one dipole field oriented in the horizontal plane and the other one oriented in the vertical plane [29,30]. The raster coils were driven by 2 kHz AC fields and phased to produce a spiral beam pattern as described in detail in Section 3.2. The raster coils were not included in the GPT simulation.

3. Beamline components

As shown schematically in Fig. 5, the main components of the irradiation beamline consist of the beam expanding solenoid and raster coils mentioned above plus two pairs of steering magnets, two beam position monitors (BPM), two beam viewer screens, one insertable Faraday cup (Fcup), the titanium foil window, the target sample positioning stage with local lead-brick radiation shielding, and beamline vacuum pumps (ion and non-evaporable getter). The inner diameter (ID) of the beam pipe upstream of the orifice is 35 mm and increasing to 63 mm downstream.

In addition to the items listed above, elements were added to the accelerator to provide "machine protection" in case of accidental venting of the beamline, for example due to a failure of the thin beam exit window. These include a commercial ultra-high vacuum fast valve system (Part No. 75232-UE44-0003, VAT, Austria), with associated pressure gauge located near the titanium foil window, and with the valve positioned as close to the SRF cryomodule as possible.

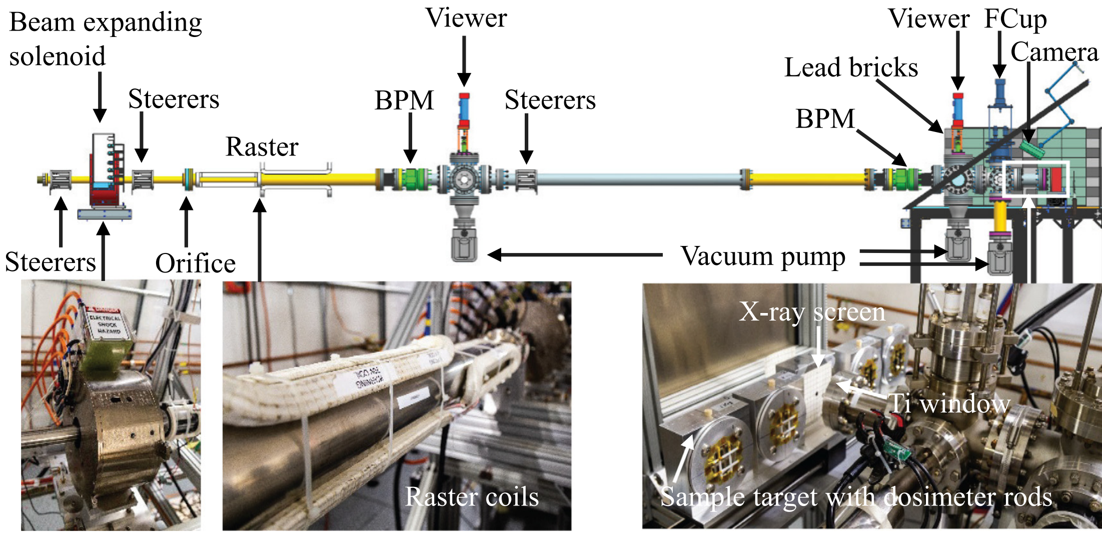

Fig. 5. Layout of EB irradiation beamline at the extended, straight section of the UITF. (BPM -- beam position monitor; Fcup -- faraday cup; Ti -- titanium-foil.)

An orifice with 16 mm diameter was also added downstream of the beam expanding solenoid, near the intended location of a beam waist, which serves as a conductance limiting device in case of failure of the beam exit window.

3.1. Beam expanding solenoid

The solenoid has an iron yoke to hold the copper coils and to clamp the field at the ends. It has an outer diameter (OD) of 27 cm, an ID of 3.4 cm, and a length of 15 cm. The inner coils are made of a hollow conductor to allow for water cooling. The axial magnetic field was measured as a function of current to the coils. The measured axial magnetic field at 100 A is in good agreement with the field map used for the GPT simulation, as shown in Fig. 6(a). The measured peak axial magnetic field, B_0, is proportional to the magnitude of the current, I_{dc}, as shown in Fig. 6(b), increasing at a rate of 2.33 mT/A. The solenoid is protected by coil temperature and cooling water flow interlocks.

3.2. Raster

A beam raster consisting of two orthogonal dipole magnet coils was installed after the beam expanding solenoid to further increase the transverse beam size in order to make a more uniform beam distribution at the sample target. As shown in Fig. 7, the air-core magnet coils are made of Litz 1650 conductor for operation at frequencies up to 100 kHz [29]. The inductance of the magnet coil is of the order 100 μH. Each coil is powered by a 1.2 kW amplifier (M600, Bogen Communications, LLC, USA) at a frequency of 13 kHz. The output of each amplifier is amplitude-modulated (AM) with an external function generator at 2 kHz frequency and with a 90° phase offset between coils. Two Pearson current monitors were used as interlocks to protect the coils during operation. The maximum AC current amplitude to each coil circuit was 15 A. The current waveforms applied to the deflection coils during one AM period are shown in Fig. 7(a), and the resulting beam distribution generated downstream of the raster after ten AM periods is shown in Fig. 7(b).

3.3. Beam exit window

A commercial Ti-foil window assembly (Part No. FWFSS-0450, Atlas Technologies, USA) was chosen for the beam exit window [31,32]. The foil is made of titanium grade 2 with a thickness 0.127 mm and an ID of 61.93 mm. Thermal and mechanical analysis of the window were carried out using the finite-element analysis software, ANSYS [33]. Considering a 1 atm differential pressure, the simulation predicted a

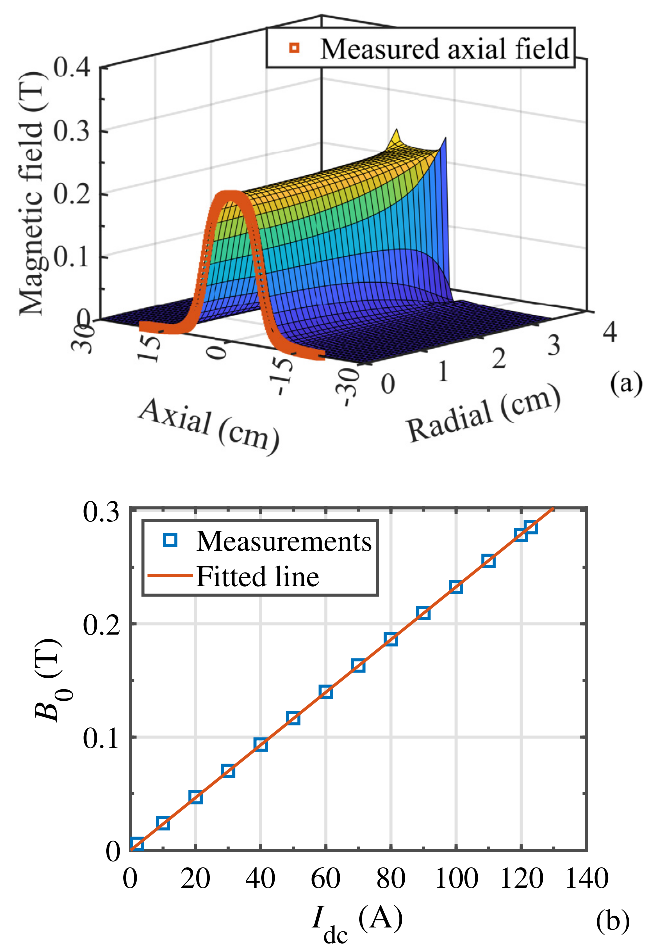

Fig. 6. Magnetic field at 100 A (a) and axial peak magnetic field as a function of DC current for the solenoid (b).

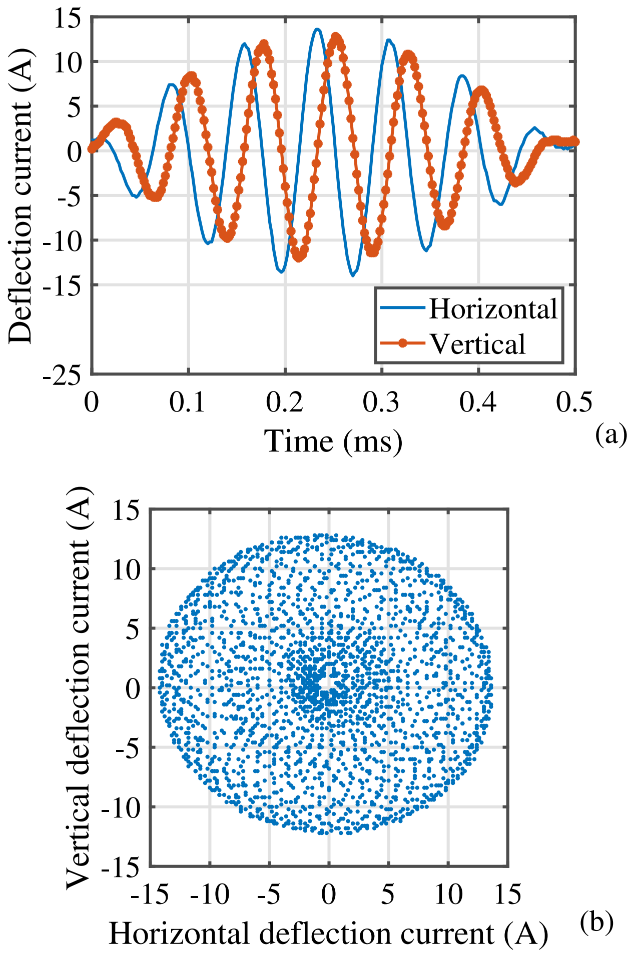

Fig. 7. Raster magnet excitation and resulting beam distribution: (a) the current waveforms applied to the raster coils during one AM period, and (b) the spiral beam pattern generated downstream after 10 AM periods.

maximum deformation of ∼1.3 mm at the center of the foil and a maximum von Mises stress of 345 MPa, less than the material's tensile strength, at the edge of the support ring.

A simulation with the Monte-Carlo software FLUKA [34] predicted that 6.9×10^{-5} W/nA will be dissipated in the titanium foil for an electron beam total energy of ∼8 MeV. A simulation was carried out with ANSYS to calculate the peak temperature of the foil as a function of beam current and σ of the beam, assuming conduction through the Ti foil and natural air convective heat transfer on the outer surface of the foil. The peak temperature in the titanium foil can also be estimated using the analytical solution of the heat diffusion equation [35]:

$$T_{\max} = \frac{P_{\mathrm{loss}}}{2\pi h_{\mathrm{air}}} \int_0^{\infty} \frac{kt\beta + \tanh(kt)k}{kt\beta + (kt\beta)^2 \tanh(kt)} e^{-k^2\sigma^2/2} \mathrm{d}k + T_0 \quad (1)$$

where $\beta = \frac{k}{t \cdot h_{\mathrm{air}}} = 2.583 \times 10^4$, $t = 0.127$ mm is the window thickness, $k = 16.4$ W/(m K) is the thermal conductivity of Ti, $h_{\mathrm{air}} = 5$ W/(m^2 K) is the natural convection coefficient of air, $T_0 = 22$ °C is the ambient temperature, σ is the standard deviation of transverse beam size and P_{loss} is the fraction of beam power dissipated in the window.

Fig. 8 shows the peak temperature in the titanium foil for two different transverse electron beam sizes from ANSYS simulations and calculated with Eq. (1). The results are consistent between one another and show that the peak temperature of the thin titanium foil is much less than the melting temperature of Ti. Even for the case of focused beam at the titanium window, with the smallest possible transverse σ of 66 μm, the peak temperature rise in the foil would be less than 3 °C

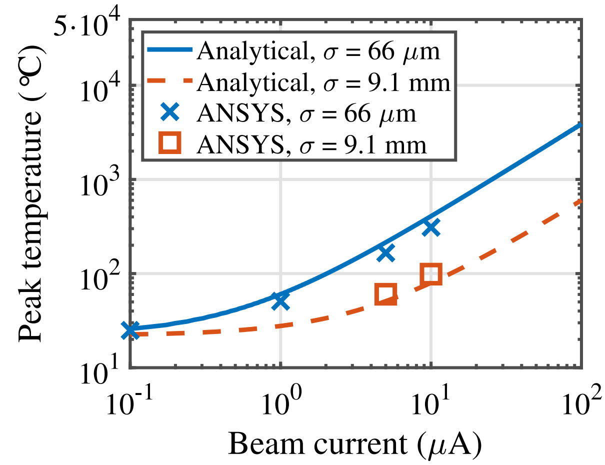

Fig. 8. Peak temperature of the titanium-foil window as a function of beam current for $E_b = 8$ MeV. Two beam sizes were considered: $\sigma = 9.1$ mm and $\sigma = 0.066$ mm (smallest achievable beam). The solid and dashed lines were obtained using Eq. (1), the individual data points were obtained from a simulation with ANSYS.

at the beam current of 100 nA, and it decreases with increasing beam size.

3.4. Irradiation target

A remotely controlled motorized linear translation stage, located ∼6 cm behind the titanium-foil window, was used to move the sample targets in front of the electron beam. The stage can hold up to five targets: four positions were used for actual target cells and one position held an X-ray fluorescent screen used to monitor the electron beam size and position before and after each EB irradiation (Fig. 5). Opti-chromic dosimeter rods were taped to the front of the targets to measure the dose during irradiation. The sample holders are cuboids made of aluminum with a square front having an edge length of 12.70 cm and 5.08 cm depth. The water sample resides in a cylindrical volume (48.5 mm diameter, 33 mm deep) cut in the aluminum block, kept in place with a stainless steel window, 0.127 mm thick, sealed to the aluminum block using a cork gasket and an aluminum ring. The radius of the sample volume was chosen to be equal to the beam radius to facilitate irradiation of the entire cross section, and the depth was chosen to be 33 mm, resulting in a volume of ∼60 mL, sufficient for post-irradiation analysis of the water samples. Fig. 9(a) shows the geometry of the sample holder and elements used for the FLUKA simulations.

The electron penetration depth depends on the electron beam energy [36–38] and Fig. 9(b) shows the dose as a function of depth in water for different beam energies, calculated with FLUKA. A beam energy of 8 MeV is a good compromise between avoiding operation close to the maximum allowed operational beam energy of 10 MeV at UITF and avoiding delivering too low of a dose at the end of the sample volume.

Although not presented in detail here, the FLUKA simulations show that an electron beam with a relative energy spread of less than 10^{-2} and a diverging angle of less than 10 mrad provides a dose distribution comparable to that of a mono-energetic electron beam with no divergence [28]. The relative energy spread at the beam exit of the beamline is of the order of 5×10^{-4} and the diverging angle is ∼4 mrad, therefore the FLUKA simulations discussed in this paper were conducted with a mono-energetic electron beam with no divergence.

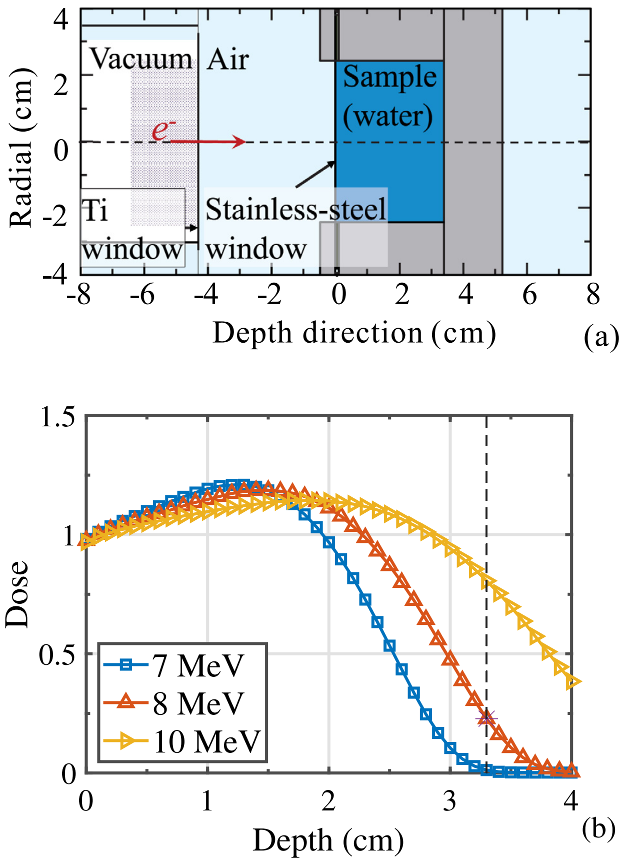

Fig. 9. Cross-section of the geometry used for the FLUKA simulations (a) and dose distributions for three different values of total electron energy, normalized to the dose value at the entrance to the water (b). The dashed line in (b) indicates the depth of the target cell.

3.5. Other components

Conventional air-core steering magnets were used to steer the electron beam. Two yttrium aluminum garnet (YAG) beam viewers could be inserted into the beampipe to determine the beam position, beam profile and beam size. Non-invasive beam position monitors (BPMs) could be used to monitor the beam position for beamline commissioning but not during sample irradiation, since the beam current for sample irradiation was too low to trigger BPMs. Ion pumps and non-evaporable getter pumps were used to maintain a beamline pressure of $\sim 10^{-8}$ mbar. The beam current was monitored using a resonant cavity beam current monitor and two insertable Faraday cups, one located at the exit of the SRF cryomodule, and another near the beam exit window. A wire scanner [39] upstream of the beam expanding solenoid was used to measure the beam size and for comparison with the beam viewers.

4. Beamline commissioning results

Commissioning of the EB irradiation beamline was performed using low-duty factor "machine safe" beam mode, at a small fraction of the beam current used for water irradiation. To create this machine-safe beam mode, the drive laser light delivered to the photo-gun was chopped using a Pockels cell to create 4 μs macropulses at 60 Hz. The average beam current in this mode was of the order 1 nA, which was high enough to illuminate the YAG viewer screens to steer the beam. The total energy of the beam used during commissioning was ∼8 MeV.

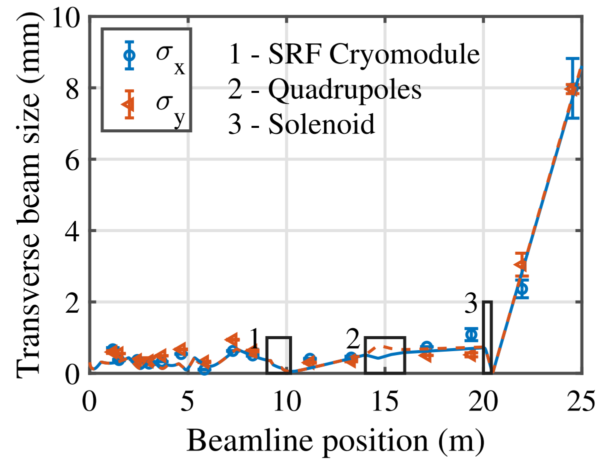

Fig. 10. Transverse beam size (1σ) along the entire accelerator beamline measured with viewer screens at fixed locations. Each data point represents the average of four measurements made days apart. The solid and dashed lines represent the transverse beam size in the x- and y-direction, respectively, as simulated with GPT.

4.1. Beamline envelope measurement

The electron beam size was measured at each viewer screen along the entire length of the accelerator beamline. There were two kinds of beam viewers: Chromox and YAG. Both fluoresce when struck by an electron beam. YAG screens are preferable because they offer more dynamic range, and the fluorescence quickly extinguishes when the electron beam is terminated (referred to as "image persistence"). The laser power delivered to the photogun was adjusted to vary the electron beam current to avoid saturating the camera image from the beam fluorescence during each beam size measurement. The viewer screen measurements of beam size agree with measurements made using wire scanners, within 10%. Possible causes for this discrepancy include the image persistence mentioned above, the camera image data rate, and assigning an accurate calibration relationship between the camera unit pixel count and the true size [40]. Fig. 10 shows the measured transverse beam size along the accelerator, without beam raster. Each data point in Fig. 10 represents the average of four measurements, made days apart but with the same accelerator settings. The relative uncertainties of the measurements are less than or close to 10%, which shows an acceptable reproducibility of the beamline setup. The magnets settings in the keV region had to be adjusted, compared to those used in the initial simulation with results shown in Fig. 2, in order to obtain a good agreement with the measurements, as shown in Fig. 10. Operation of the solenoid with 110 A (0.25 T peak axial magnetic field) resulted in a transverse beam size (1σ) of ∼8 mm in both planes at the last viewer location, immediately upstream of the beam exit window, in good agreement with beam transport simulations.

4.2. Beam on the irradiation target

It is important to measure the transverse beam size at the target position for an accurate calculation of the dose distribution inside sample. This was realized using an X-ray screen placed in front of the "dummy" target sample holder consisting of a solid Al block. Fig. 11 shows camera images of the fluorescent X-ray screen, providing an indirect image of the electron beam, with and without the beam raster. The intensity was more diffused with the raster coils energized, as expected. The horizontal projection is parallel to the camera capture plane, and the fitted σ_x was ∼15 mm. The σ of vertical projection of the X-ray image, σ_y, was also ∼15 mm after correcting for the 70° angle between the X-ray screen and the camera plane.

Fig. 12 shows that the horizontal beam size increases linearly with the current amplitude of the horizontal deflection raster coils, which

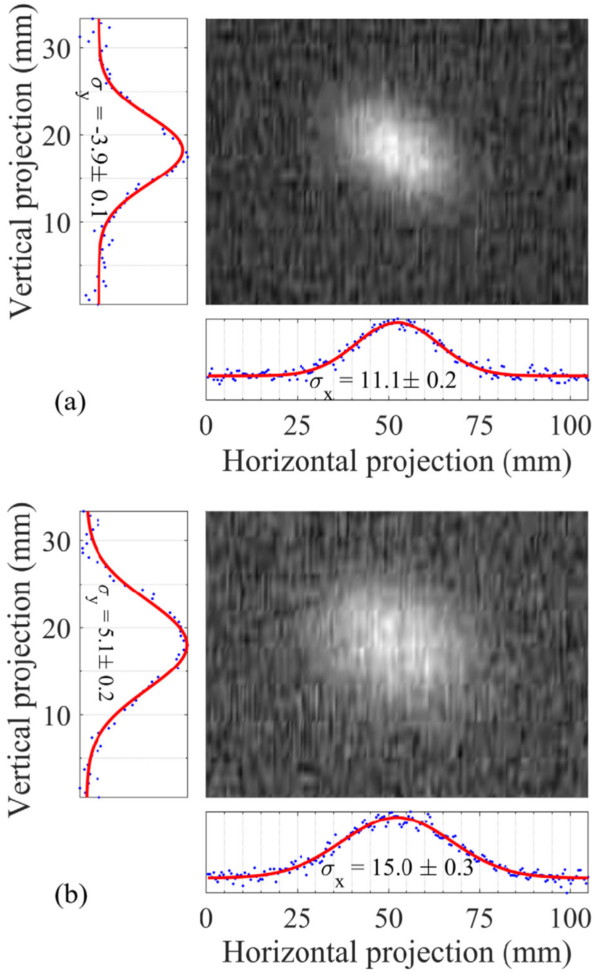

Fig. 11. Electron beam images on the X-ray screen at the target location with raster off (a) and on (b). The beam size σ shown in the figure is in mm.

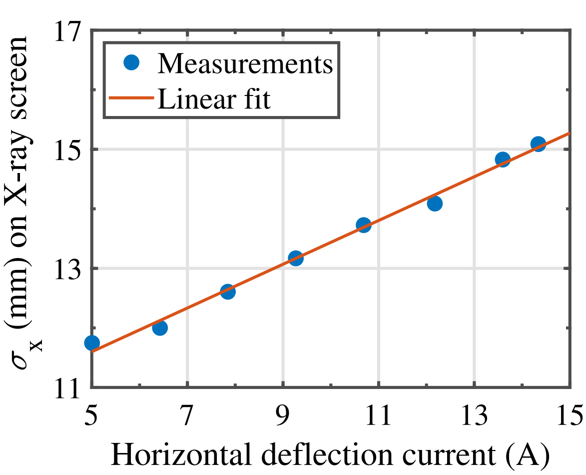

Fig. 12. Horizontal beam size on the X-ray screen as a function of the horizontal raster deflection coil current. Similar results were obtained in the y-plane using the vertical raster coils.

is expected since a higher raster coil current increases the diameter of the pattern in Fig. 7(b). Given the measured $\sigma \simeq 15$ mm of the beam at the target location, FLUKA simulations show that ~90% of the electrons were delivered to the sample cross section.

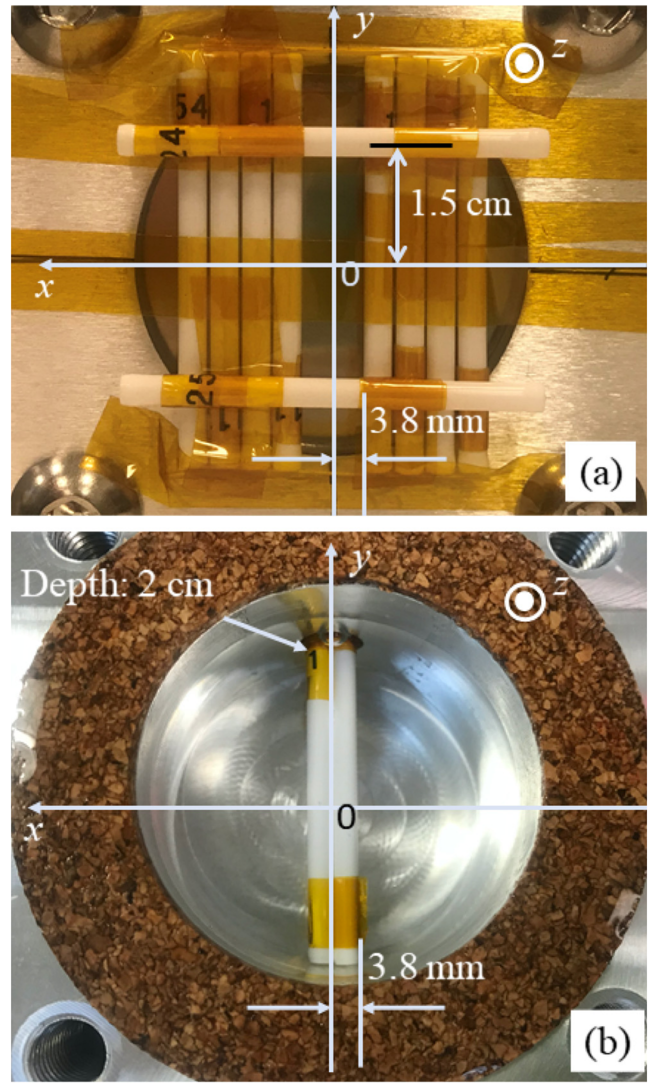

Fig. 13. Dose mapping setup with ten rods in front of the target cell's stainless steel window (a) and two rods at 2 cm depth inside the sample volume (b).

5. Dosimetry methodology and 1,4-dioxane sample irradiation

The dose delivered to the sample volume plays an important role in the assessment of EB treatment efficacy, but it is difficult to measure directly. Some studies have used calorimetric methods [41,42] while others have used alanine dosimeters inside or outside the samples [9]. In our case, the temperature rise in the water resulting from the irradiation is too small to be measured accurately and alanine dosimeters require an expensive spin spectrometer instrument for dose readout. The approach we chose was to combine simulation data for the full sample volume with dose measurements at specific locations inside and outside the sample chamber. Opti-chromic dosimeter rods (FWT-70-40M, Far West Technology Inc., Goleta, GA, USA) were used to measure a dose of up to 10 kGy at each specific location. The dosimeter rods are ~5 cm long and 3.8 mm in diameter. Eight rods were taped vertically and two horizontally at the front of the target cell, with a gap between the vertical rods in the center to allow full irradiation of two additional dosimeter rods inside the sample volume. Fig. 13 shows images of the setup for dose mapping.

FLUKA simulation provides dose rate values at any location of the elements used in the simulation, as well as the integrated dose rate over the sample volume. EB irradiation of targets filled with tap water

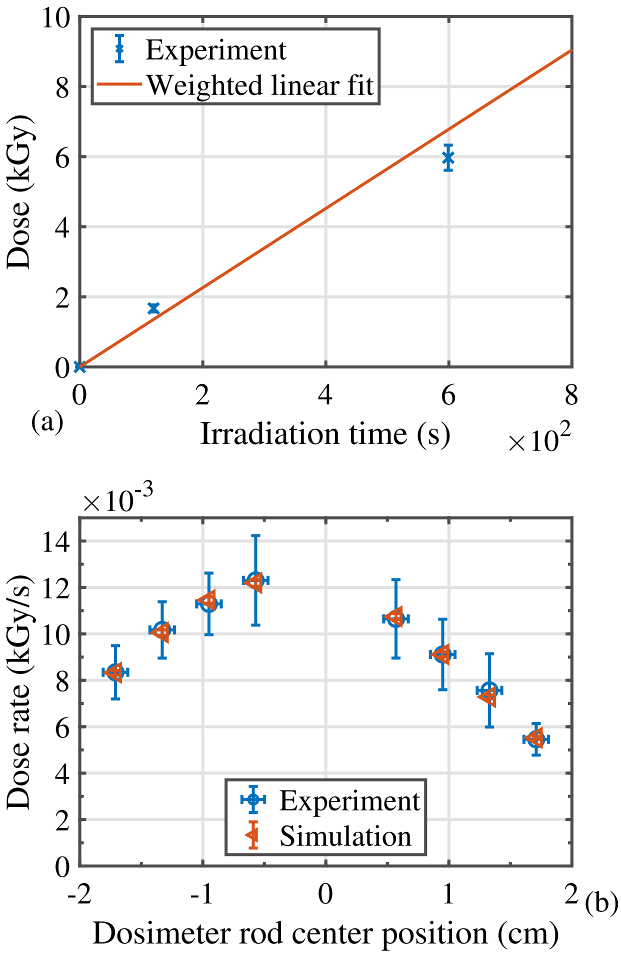

Fig. 14. (a) Dose versus irradiation time measured by the vertical dosimeter rod located at $x = -0.95$ cm from the center and (b) comparison of dose rates measured by the vertical dosimeter rods placed in front of the target window with those calculated by FLUKA.

were done for 2 min and 10 min, using the dose mapping setup shown in Fig. 13. After irradiation, the dosimeter rods were kept in a dark container for ∼24 h before being read by an opti-chromic dose reader (FWT-200S, Far West Technology Inc., Goleta, GA, USA). They were evaluated again after 72 h and there was no significant change in the dose values compared to the previous measurement.

Fig. 14(a) shows, as an example, the measured dose as a function of irradiation duration for the dosimeter rod located at $x = -0.95$ cm. The dose rate is given by the slope of a weighted least-squares linear fit of the data. Similarly, the dose rates at all other rod positions were obtained. The transverse beam size, the beam center position and a dose rate scale factor α in the FLUKA simulation were considered as parameters to minimize the sum of the squared errors of the dose rates at the 12 measured locations. The scale factor accounts for systematic uncertainties both in the Monte-Carlo simulation, such as those related to the physics models, transport algorithm and cross section data, as well as those related to differences between the model setup and the real components [34]. The values of the fit parameters were σ = 15.3 mm, the beam center position with respect to the center of the target was $x_c = -3.0$ mm, $y_c = 1.7$ mm and the scale factor was 1.30. This small off-center shift of the beam gives an indication of the accuracy in centering the beam on the target in our setup. The measured beam energy, $E_b = 8$ MeV, and beam current, $I_b = 108$ nA, were kept as fixed parameters in the FLUKA simulation.

Following the dose mapping study, four dosimeter rods, two in the vertical and two in the horizontal direction, at ±1 cm from the target center, were taped in front of the target window, as shown in the sample target layout picture in Fig. 5. This helps confirming that the beam was properly centered during sample irradiation, and verifying the calculated dose at those locations. A total of 58 samples with different 1,4-dioxane initial concentrations and water matrices were irradiated for durations ranging between 0.5 − 40 min. A comparison of the dose rates measured by the four dosimeters with those calculated by FLUKA, with the beam size and scale factor determined from the dose mapping study discussed above, resulted in an average beam center position of $x_c = -5 \pm 1$ mm and $y_c = -1 \pm 1$ mm. An average beam energy of 8 MeV and an average beam current of 108 nA were measured over the irradiation of all samples. The total dose, D, delivered to the sample was calculated as:

$$D = \frac{dD}{dt} I_b t_b \tag{2}$$

where t_b is the irradiation time and $dD/dt = 0.54$ kGy/min is the integrated dose rate over the sample volume calculated by FLUKA with $E_b = 8$ MeV, $I_b = 108$ nA, $(x_c, y_c) = (-5\text{ mm}, -1\text{ mm})$, $\sigma = 15.3$ mm and $\alpha = 1.3$. Fig. 15(a) shows the 2D dose distribution within the water sample volume calculated with FLUKA, using this set of parameters. The sample volume fraction as a function of normalized dose fraction is shown in Fig. 15(b). About 65% of the sample volume receives between 27 − 63% of the peak dose. In addition, the simulation results showed that ∼54% of the beam power was delivered to the water sample volume and ∼39% to the sample chamber.

The relative uncertainty of the absorbed dose is between 3.0 − 5.0%. It includes the uncertainties in the measurements of time (1 s), beam current (0.3 − 1.4%) and the calculated dose rate (∼3%). The uncertainty in the calculated dose rate includes the uncertainty in the beam center position (∼1.1%), the root mean square deviation between the dose rates of the 12 dosimeter rods and those from the simulation (∼1.1%), and the average uncertainty (∼2.5%) of the experimental dose rates of the 12 dosimeter rods.

Fig. 16 shows, as an example, the relative concentration of 1,4-dioxane in ultra-pure water (UPW) as a function of dose, for two initial concentration values. About 95% of 1,4-dioxane was removed with a dose of ∼1 kGy for both samples. All of the experimental data on 1,4-dioxane removal as a function of dose, initial concentration and water matrix will be discussed in an upcoming publication [43].

6. Summary and outlook

An irradiation beamline at the UITF accelerator at Jefferson Lab was successfully designed, installed and commissioned. It allows for EB irradiation of up to five targets on a linear rail with a Gaussian beam with a transverse beam size (1σ) of ∼15 mm at the target position, a beam energy of up to 10 MeV and a beam current of ∼100 nA. We achieved the large beam size at the target location mainly by using a defocusing solenoid, instead of the more traditional rastering of a small beam. The maximum beam power is currently limited by the amount of concrete shielding present at the facility, which is planned to be increased in the near future, allowing higher beam current by a factor of at least ten. Even though the available beam power is much less than that of accelerators used for environmental remediation, the establishment of the beamline described in this article is a significant accomplishment in two main aspects: (i) it adds to the very limited number of facilities in the US capable of conducting R&D with EB radiation and (ii) it provides a proof of feasibility of using an SRF accelerator for this kind of applications. Recent advances in SRF accelerator technologies provide a positive outlook towards realizing efficient, low cost, high power electron accelerators for industrial applications in the coming years.

We have also presented a detailed characterization of the dose distribution achieved by combining FLUKA simulations with dose mapping using low-cost dosimeters. We have established a collaboration with the local wastewater treatment utility company to investigate the

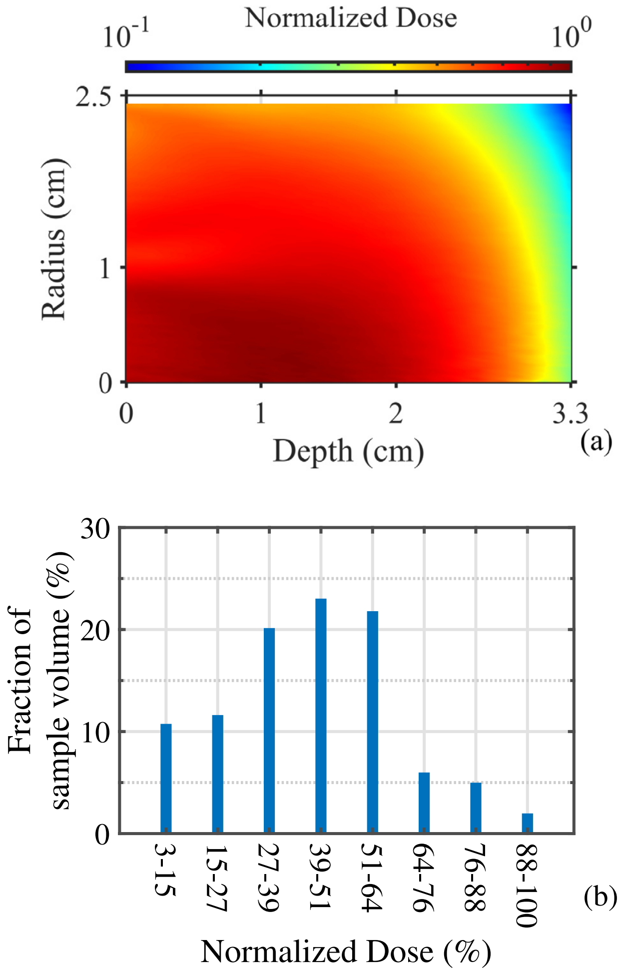

Fig. 15. 2D dose distribution within the water sample (a) and sample volume fraction as a function of the dose normalized to the peak value (b) calculated with FLUKA.

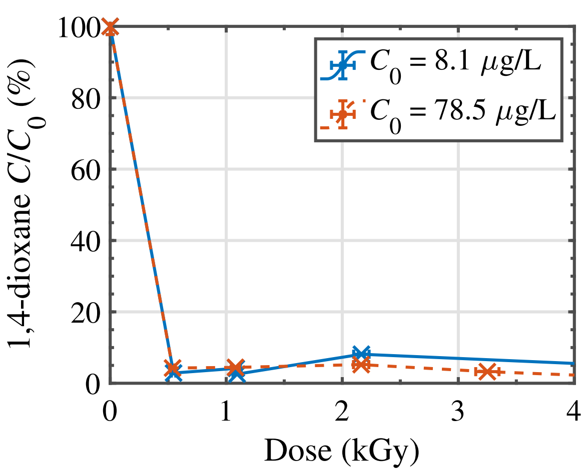

Fig. 16. Relative concentration of 1,4-dioxane in ultra-pure water as a function of the absorbed dose. C_0 and C are 1,4-dioxane concentrations in UPW before and after EB irradiation, respectively. Error bars are the same size or smaller than the symbols. The solid and dashed lines are a guide to the eye. The concentration detection limit is 0.375 μg/L.

effect of EB irradiation on 1,4-dioxane, a chemical which is difficult to remove by conventional methods. Whereas all of the results will be presented and discussed in details in an upcoming publication, the set of results presented in this article already show the potential of EB irradiation towards eliminating such chemical with a relatively low dose. In the near future we plan to continue using the established beamline to study the effects of EB irradiation on PFAS, an even more challenging class of man-made chemicals.

Declaration of competing interest

The authors declare that they have no known competing financial interests or personal relationships that could have appeared to influence the work reported in this paper.

Data availability

Data will be made available on request.

Acknowledgments

The authors would like to thank many colleagues from the Accelerator and Engineering Divisions at Jefferson Lab for their support and contribution to the installation and commissioning of the beamline. We would also like to thank the Radiological Control group at Jefferson Lab for assisting with the dosimeters evaluation. The research was authored by Jefferson Science Associates, LLC under U.S. DOE Contract No. DE-AC05-06OR23177 and supported by a Laboratory Directed Research and Development grant, United States.

References

[1] C. Kurucz, T. Waite, W. Coopers, The miami electron beam research facility: a large scale wastewater treatment application, Radiat. Phys. Chem 45 (2) (1995) 299–308.
[2] R.W. Hamm, M.E. Hamm, Industrial Accelerators and their Applications, World Scientific, Singapore; Hackensack, NJ, 2012.
[3] B. Han, S. Sabharwal, W. Ellison, A.G. Chmielewski (Eds.), Radiation processing: environmental applications, in: ISBN 92-0-100507-5, IAEA, Vienna, 2007.
[4] Industrial Radiation with Electron Beams and X-rays, Tech. rep., International irradiation association, 2011.
[5] W.J. Cooper, R.D. Curry, K.E. O'Shea (Eds.), Environmental Applications of Ionizing Radiation, John Wiley & Sons, New York, 1998.
[6] M. Siwek, T. Edgecock, Application of electron beam water radiolysis for sewage sludge treatment—a review, Environ. Sci. Pollut. Res. 27 (2020) 42424–42448.
[7] C. Kurucz, T. Waite, W. Cooper, M. Nickelsen, High energy electron beam irradiation of water, wastewater and sludge, Adv. Nucl. Sci. Technol. 22 (1991) 1–43.
[8] https://www.niehs.nih.gov/health/materials/perfluoroalkyl_and_polyfluoroalkyl_substances_508.pdf.
[9] L. Wang, B. Batchelor, S.D. Pillai, V.S.V. Botlaguduru, Electron beam treatment for potable water reuse: Removal of bromate and perfluorooctanoic acid, Chem. Eng. J. 302 (2016) 58–68.
[10] M. Trojanowicz, I. Bartosiewicz, A. Bojanowska-Czajka, K. Kulisa, T. Szreder, K. Bobrowski, H. Nichipor, J.F. Garcia-Reyes, G. Nalecz-Jawecki, S. Meczynska-Wielgosz, J. Kisala, Application of ionizing radiation in decomposition of perfluorooctanoate (PFOA) in waters, Chem. Eng. J. 357 (2019) 698–714, http://dx.doi.org/10.1016/j.cej.2018.09.065, URL https://www.sciencedirect.com/science/article/pii/S1385894718317820.
[11] M. Trojanowicz, I. Bartosiewicz, A. Bojanowska-Czajka, T. Szreder, K. Bobrowski, G. Nalecz-Jawecki, S. Meczynska-Wielgosz, H. Nichipor, Application of ionizing radiation in decomposition of perfluorooctane sulfonate (PFOS) in aqueous solutions, Chem. Eng. J. 379 (2020) 122303, http://dx.doi.org/10.1016/j.cej.2019.122303, URL https://www.sciencedirect.com/science/article/pii/S1385894719316973.
[12] T.H. Kim, S. Yu, Y. Choi, T. Jeong, S. Kim, Profiling the decomposition products of perfluorooctane sulfonate (PFOS) irradiated using an electron beam, Sci. Total Environ. 631–632 (2018) 1295–1303, http://dx.doi.org/10.1016/j.scitotenv.2018.03.055.
[13] K. Londhe, C. Lee, Y. Zhang, S. Grdanovska, T. Kroc, C.A. Cooper, A.K. Venkatesan, Energy evaluation of electron beam treatment of perfluoroalkyl substances in water: A critical review, ACS EST Eng. 1 (2021) 827–841.
[14] D. Gonzalez, K. Thompson, O. Quiñones, E. Dickenson, C. Bott, Granular activated carbon-based treatment and mobility of per- and polyfluoroalkyl substances in potable reuse for aquifer recharge, AWWA Water Sci. (2021) e1247.

[15] https://www.epa.gov/sites/default/files/2014-03/documents/ffrro_factsheet_contaminant_14-dioxane_january2014_final.pdf.
[16] U.S. EPA, Announcement of preliminary regulatory determinations for contaminants on the fourth drinking water contaminant candidate list, Federal register 85 (47) (2020) 14098–14142.
[17] R.A. Salimov, High power DC electron accelerators of the ELV type, AIP Conf. Proc. 592 (1) (2001) 580–600, http://dx.doi.org/10.1063/1.1420431.
[18] https://eb-tech.com/en/.
[19] https://www.ans.org/news/article-3073/chinas-electron-beam-technology-for-treating-industrial-wastewater/.
[20] http://www.dasheng.com/en/dd.html.
[21] S. Henderson, T. Waite (Eds.), Workshop on Energy and Environmental Applications of Accelerators, Argonne, IL, USA, Department of Energy, 2015.
[22] H. Padamsee, 50 Years of success for SRF accelerators—a review, Supercond. Sci. Technol. 30 (5) (2017) 053003, http://dx.doi.org/10.1088/1361-6668/aa6376.
[23] G. Ciovati, J. Anderson, B. Coriton, J. Guo, F. Hannon, L. Holland, M. LeSher, F. Marhauser, J. Rathke, R. Rimmer, T. Schultheiss, V. Vylet, Design of a cw, low-energy, high-power superconducting linac for environmental applications, Phys. Rev. Accel. Beams 21 (2018) 091601, http://dx.doi.org/10.1103/PhysRevAccelBeams.21.091601.
[24] R.C. Dhuley, I. Gonin, S. Kazakov, T. Khabiboulline, A. Sukhanov, V. Yakovlev, A. Saini, N. Solyak, A. Sauers, J.C.T. Thangaraj, K. Zeller, B. Coriton, R. Kostin, Design of a 10 MeV, 1000 kW average power electron-beam accelerator for wastewater treatment applications, Phys. Rev. Accel. Beams 25 (2022) 041601, http://dx.doi.org/10.1103/PhysRevAccelBeams.25.041601, URL https://link.aps.org/doi/10.1103/PhysRevAccelBeams.25.041601.
[25] Y. Wang, P. Adderley, M. Bruker, C.H. Garcia, J. Grames, S. Gregory, J. Hansknecht, X. Li, M. McCaughan, M. Poelker, M. Stutzman, D. Turner, The upgraded injector test facility at Jefferson lab, 2022, in preparation.
[26] S.B. van der Geer, M.J. de Loos, General particle tracer: a 3D code for accelerator and beamline design, in: Proceedings of 1998 European Particle Accelerator Conference, EPAC'98, JACoW, Stockholm, Sweden, 1998, p. 1245.
[27] F. Hannon, A high Average-current Electron Source for the Jefferson laboratory free electron laser (Ph.D. thesis), University of Lancaster, UK, 2008.
[28] X. Li, H. Baumgart, G. Ciovati, F. Hannon, S. Wang, Simulation studies on the interactions of electron beam with wastewater, in: Proc. 12th Int. Particle Accelerator Conf., IPAC'21, Campinas, Brazil, 2021, http://dx.doi.org/10.18429/JACoW-IPAC2021-WEPAB255.
[29] C. Bass, Development of fast rasters for eHD test runs and experiments, Tech. rep., Jefferson lab, 2013.
[30] C. Yan, N. Sinkine, R. Wojcik, Linear beam raster for cryogenic targets, Nucl. Instrum. Methods Phys. Res. A 539 (2005) 1–15.
[31] https://www.atlasuhv.com/products/aluminum-titanium-flanges/foil-window-flange/.
[32] http://www.matweb.com/search/DataSheet.aspx?MatGUID=49a4b764217b44ee953205822af5fbc9&ckck=1.
[33] https://www.ansys.com/products/structures/ansys-mechanical.
[34] https://fluka.cern/.
[35] A. Gurevich, G. Ciovati, Effect of vortex hotspots on the radio-frequency surface resistance of superconductors, Phys. Rev. B 87 (5) (2013) 054502.
[36] Linear Energy transfer, Tech. rep., International Commission on Radiation Units and Measurements, Washington, D.C. 20008, USA, 1970.
[37] M.J. Berger, S.M. Seltzer, Tables of energy losses and ranges of electrons and positrons, Tech. rep., Scientific and Technical Information Division, National Aeronautics and Space Administration, Washington, D.C. 20230, USA, 1964.
[38] R. Miller, Electronic Irradiation of Foods: An Introduction to the Technology, Springer Science Business Media, Inc., Albuquerque, NM, USA, 2005.
[39] https://www.jlab.org/accel/beam_diag/harp/harp_dummy.html.
[40] X. Li, Beam size measurement with view screen at UITF, Tech. rep. JLAB-TN-22-006, Jefferson lab, 2022.
[41] T.D. Waite, C.N. Kurucz, W.J. Cooper, D. Brown, Full scale electron beam systems for treatment of water, wastewater and medical waste, Tech. rep. IAEA-TECDOC–1023, International Atomic Energy Agency, 1998.
[42] M. Emami-Meibodi, M. Parsaeian, R. Amraei, et al., An experimental investigation of wastewater treatment using electron beam irradiation, Radiat. Phys. Chem. 125 (2016) 82–87.
[43] R. Pearce, C. Bott, G. Ciovati, X. Li, H. Vennekate, Electron-beam treatment for the removal of 1,4-dioxane in water and wastewater treatment, 2022, in preparation.